Supporting Information for

Dynamics and control of gold-encapped gallium arsenide nanowires imaged by 4D electron microscopy

Bin Chen,[1,*] Xuewen Fu,[1] Jau Tang,[1,*] Mykhaylo Lysevych,[2] Hark Hoe Tan,[3] Chennupati Jagadish,[3] Ahmed H. Zewail[1,†]

[1]Physical Biology Center for Ultrafast Science and Technology, Arthur Amos Noyes Laboratory of Chemical Physics, California Institute of Technology, Pasadena, CA 91125, USA

[2]Australian National Fabrication Facility, Research School of Physics and Engineering, The Australian National University, Canberra, ACT 2601, Australia

[3]Department of Electronic Materials Engineering, Research School of Physics and Engineering, The Australian National University, Canberra, ACT 2601, Australia

*Corresponding author. Email: bchen5@caltech.edu, jautang@caltech.edu

[†]Deceased

The PDF file includes:

Supporting Notes

Sample preparation for electron microscopy imaging

The free-standing nanowires (NWs) still intact on the substrate were mounted on a double-tilt holder (Fig. S1A). A magnified image of the sample (marked by a rectangular box) is shown in Fig. S1B. The sample preparation is schematically illustrated in Fig. S1C. One thickness (~0.3 mm) side of the substrate (typical dimensions of ~2×1×0.3 mm^3) was glued on a Cu O-ring. Fig. S1D shows a typical transmission electron microscopy (TEM) image of the NWs (with substrate). The substrate was seen as completely dark contrast because no electron beam was transmitted.

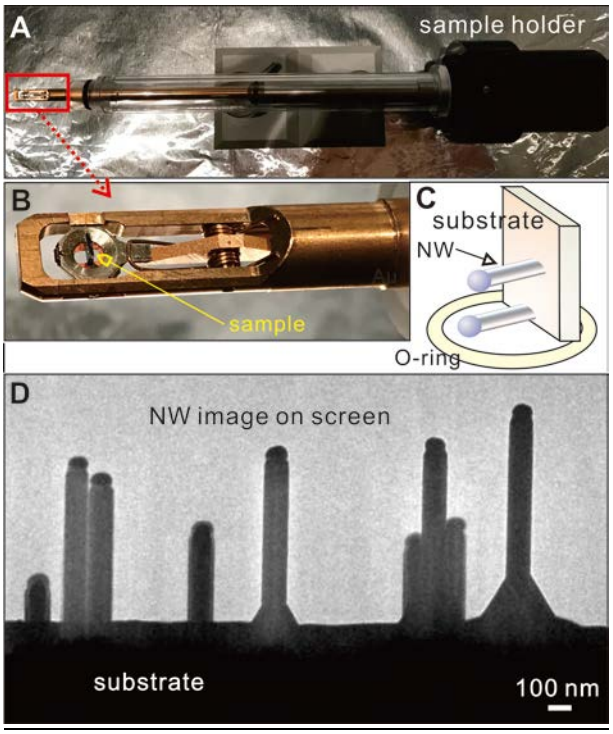

Fig. S1. Free-standing sample preparation for electron microscopy investigation. (**A**) Overview of a sample holder. (**B**) Specimen was mounted on the sample holder. This magnified image was from the box shown in (**A)**. (**C**) Schematic diagram of the free-standing NW sample preparation. (**D**) TEM image of the NWs viewed by a charge-coupled device (CCD).

Length change of the NW

Transient morphological changes of the Au/GaAs NWs were imaged in the single-pulse mode. The lengths of the GaAs NW (without the top bead) before and after laser pulse excitation are marked by white rulers (Fig. S2). In order to enhance the contrast between the top bead and the GaAs NW, and to make a comparison of the NW at different excitation stages, two reference images were taken with exposure to 100 electron pulses. One was before the arrival of a laser pulse while the other one was after the whole process ended (immediately after an incoming laser pulse an intermediate state at each delay time was captured. Then the shutter of the pump laser was closed, and we took the final reference image. This final image meant the one after the process ended). By such a way, the length of the GaAs NW at each stage was indicated by a ruler (Figs. 3 and 4 of the main text).

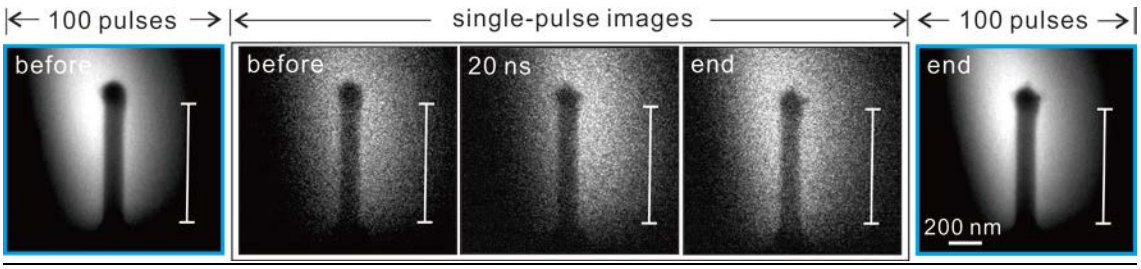

Fig. S2. Length reduction of the NW during laser pulse excitation. Intermediate state of the NW at a specific delay time was visualized by single-pulse method. To enhance the contrast and to make a clear comparison, two reference images were taken with 100 electron pulses at the stage before the excitation and after the process ended.

Width change of the NW

Fig. S3 shows a comparison between two TEM images of a NW. These two images correspond to the initial and final state of the NW, respectively. Because GaAs NW was incorporated into the top Au

bead that enabled the eutectic reactions, the top bead became bigger than the initial one. However, it is noteworthy that the width of the NW body shows no obvious change.

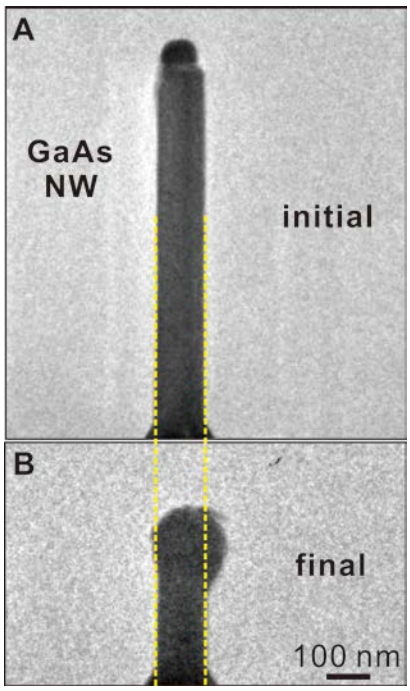

Fig. S3. TEM images of a NW, before (**A**) *vs*. after laser excitation (**B**). The dashed lines indicate the left and right edges of the NW.

Volume change of the NW

The volume change of the NW was estimated according to the schematics shown in Fig. S4. GaAs has a hexagonal shape in cross-sectional geometry (1) while the initial Au bead shows a segment shape of a sphere. The initial volume V_0 of the Au/GaAs is,

$$V_0 = S \times l + 4/3\,\pi R^3 - \pi(R-m)^2 \times (R - \tfrac{R-m}{3}) \quad (1)$$

where l and S are the length and cross-sectional area of GaAs, R is the initial radius of the Au bead and m is the height from the center point to the bottom of the sphere segment. Based on the hexagonal geometry, S equals to $\frac{3\sqrt{3}}{2}d^2$, where d is the half width of the GaAs NW.

The volume reduction of the GaAs NW as a result of the length shrinkage Δl becomes,

$$\Delta V_1 = \Delta l \times S \tag{2}$$

The volume increase of the top bead with a final radius of R' is given by,

$$\Delta V_2 = 4/3\,\pi R'^3 - [4/3\,\pi R^3 - \pi(R-m)^2 \times \left(R - \tfrac{R-m}{3}\right)] \tag{3}$$

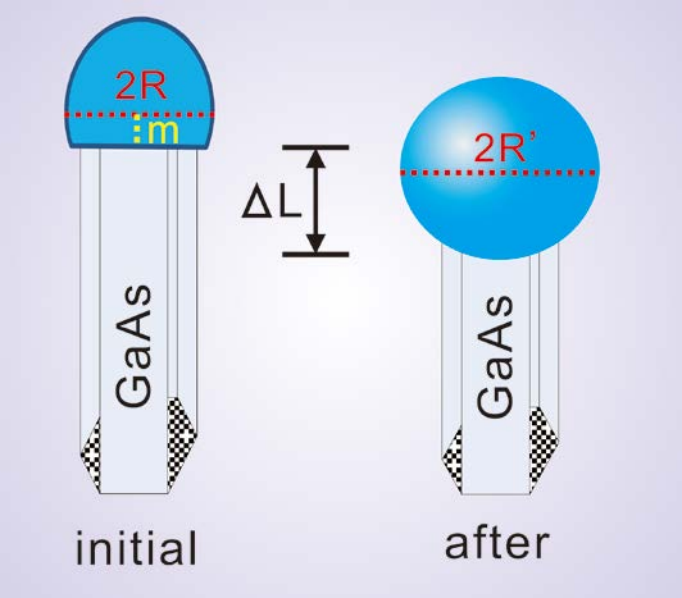

Fig. S4. Schematic diagram of the NW and the bead used for estimation of the volume changes. GaAs has a hexagonal cross-section with an area of S. The length change Δl of GaAs was measured by the difference between the initial length and the one after a laser shot. The initial Au bead shows a segment of a sphere with a diameter and height of $2R$ and $(R+m)$, respectively. The top bead after laser excitation is assumed to be a sphere with a diameter of $2R'$.

Therefore, the total volume change of the Au/GaAs is written as,

$$\Delta V = \Delta V_1 + \Delta V_2 \tag{4}$$

Substituting the parameters l, Δl, R, R', m, and d measured from the TEM images into equations (1)-(4), the volume changes of the bead and the NW are plotted in Fig. 3 of the main text.

Newly formed alloy phases after laser excitation

We applied electron diffraction to examine the newly formed alloy phases. Fig. S5 show the electron microscopy (EM) micrograph and diffraction patterns of a NW took at different modes. A region marked by a circle in Fig. S5A was used for performing the electron diffraction patterns (Fig. S5B). Three modes, namely, TEM, stroboscopic (1 kHz) and single-pulse modes were used for comparison. When the exposure time was 5 s in the TEM mode, clear diffraction spots from the sample appeared. In the stroboscopic mode, similar diffraction spots were present when the exposure time was largely increased to 120 s (only several diffraction spots appeared at the exposure time of 10 s, but with much weaker intensity due to lower electron dose). In the single-pulse mode (only a single electron pulse), however, no clear diffraction spot was observed. The reason is shown below. There are only ~10^5 electrons in a single electron pulse of the single-pulse mode (effective exposure time of only 10 ns, which is the duration of the electron pulse). Compared to the stroboscopic mode (showing the clear diffraction spots), whose repetition rate and exposure time were 1 kHz and 120 s, respectively, the electron dose in the single-pulse mode was about five orders of magnitude lower. Note that increasing the exposure time in the single-pulse mode did not help because only a single electron pulse (10 ns duration) was present for probing the sample. So current 4D EM facility is not accessible to the irreversible transient diffraction studies (single-pulse mode) of the NWs with small quantity at the nanometer-nanosecond spatiotemporal resolution shown in this work. Therefore, the newly formed alloy phases were identified in the TEM mode shown in the following part.

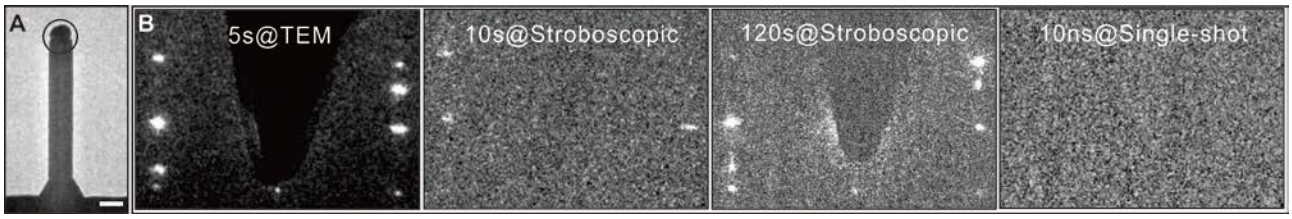

Fig. S5. Image and diffraction patterns from the top part of a NW. (**A**) TEM micrograph of the NW. Scale bar, 100 nm. (**B**) Diffraction patterns from a region of the NW marked by a circle. They were taken at three different modes: TEM, stroboscopic (1 kHz) and single-pulse modes. Different exposure times to the electron beam were applied, and the patterns at these exposure times were compared. For the single-pulse mode, the effective exposure time was only about 10 ns (duration of an electron pulse).

Fig. S6 show the diffraction patterns of the top part of a NW before and after the laser excitation. These images were taken under the off-axis conditions so that the diffraction intensities from the newly formed phases were enhanced. In the initial state (Fig. S6A), the diffraction spots were from GaAs, similar to that shown in Fig. 2 of the main text. After the first three laser pulses, however, additional diffraction spots were seen (Fig. S6B). These spots were from Au_7Ga_2 $\{11\bar{2}4\}$ (Au_7Ga_2-L, low-temperature phase) and AuGa $\{200\}$, respectively. The lattice constants used for the identification of these phases are listed in Table S1. In the final state (Fig. S6C), namely, as more GaAs component was incorporated into the top bead, new phases from $AuGa_2$ $\{111\}$ and Ga $\{131\}$ were detected besides the AuGa phase. Compared to the patterns in Fig. 2 of the main text, the diffraction spots from cubic zinc-blende (ZB) segments also appeared after laser excitation (indicated by the arrows). For the As element, the As species may vaporize or be removed from the interface during the laser heating (6, 7).

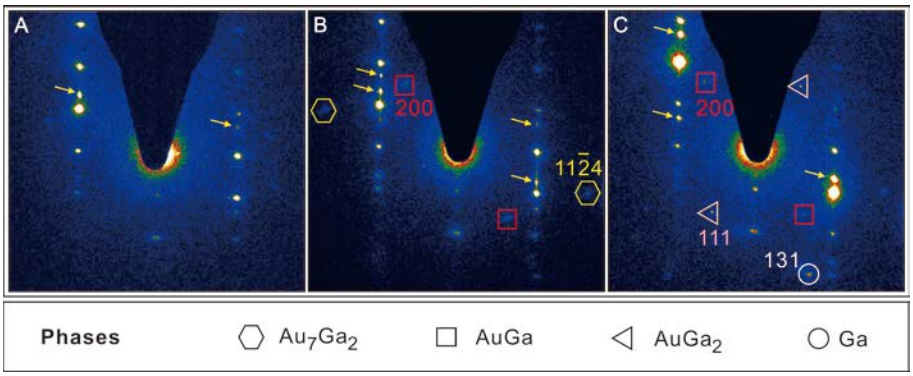

Fig. S6. Diffraction patterns from the top part of a NW. (**A**) Initial state without any laser pulse excitation. (**B**) After the first three laser pulses. Compared to the initial state in (**A**), additional diffraction spots from Au_7Ga_2 and AuGa were detected. (**C**) Final state after 46 laser pulses. AuGa, $AuGa_2$ and Ga phases were present. The hexagonal, rectangular, triangular and circular symbols represent the phases of Au_7Ga_2, AuGa, $AuGa_2$ and Ga, respectively. The arrows indicate the diffraction spots from the ZB segments of GaAs.

Table S1. Lattice constants of the newly formed phases.

Phase	**Structure**	**a** (Å)	**b** (Å)	**c** (Å)	**Reference**
Au_7Ga_2	Hexagonal	7.721	/	8.751	(2-5)
AuGa	Orthorhombic	6.397	6.262	3.463	
$AuGa_2$	Cubic	6.076	/	/	
Ga	Orthorhombic	4.519	7.657	4.526	

Phase diagram of Au-Ga binary system

From the diffraction analysis the newly formed phases in the top bead are identified as Au-Ga alloys. Fig. S7 presents the Au-Ga binary phase diagram (8). The melting points of Au and GaAs are

1337 and 1511 K, respectively. However, the temperature needed for the eutectic reaction can be much lower than the melting point of any pure component. For example, to obtain the phases of Au_7Ga_2 (low-temperature phase, Au_7Ga_2-LT) and AuGa, the temperatures are ~555 and 620 K, respectively. On the other hand, the temperature needed for the eutectic reaction of liquid → AuGa + $AuGa_2$ is about 725 K.

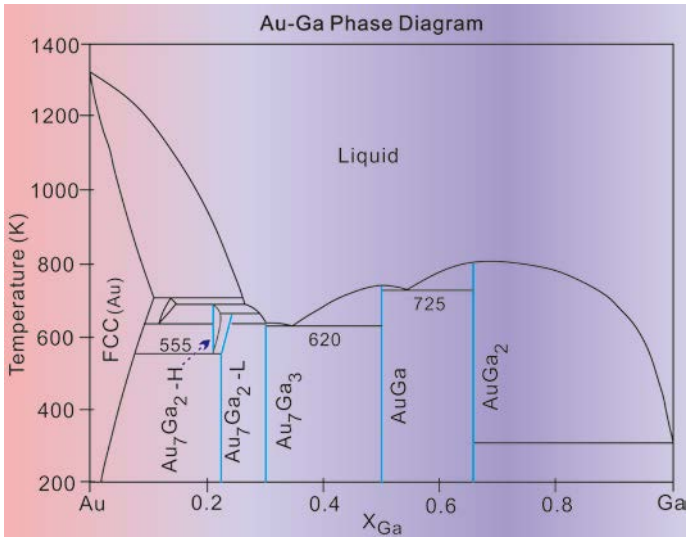

Fig. S7. Au-Ga binary phase diagram redrawn from ref. 8. The horizontal axis is the atomic fraction of Ga component.

Modeling of laser heating of gold and GaAs

Laser heating of a GaAs NW with a Au tip and the induced eutectic phase reaction can be modeled using the following theoretical approach. First, we consider laser heating of Au nanoparticle alone using the conventional two-temperature model (TTM) which deals with temporal and spatial temperature changes for both electron and phonon subsystems. Then, we treat laser heating of a GaAs NW using a three-temperature model (3TM) to deal with the temporal and spatial evolution of charged carrier density, carrier temperature, optical phonon temperature and acoustic phonon temperature. Because the optical reflectivity could be influenced by the nanoparticle size (Fig. S8), in our simulations for a given bead size we have incorporated empirical size-dependent reflectivity reported in literature (9-15). To

calculate the lattice temperature for the bead with a mixture of Au and alloy, the following approach was used. We first calculated the lattice temperature for a bead of Au (assuming 100% Au) and also a bead of GaAs (100% GaAs), and then we estimated the effective lattice temperature based on their composition percentage within the bead. This approximation is a necessary step in the simulation because the actual optical and thermal parameters used in TTM and 3TM modeling for a composite nanoparticle have not been known in literature.

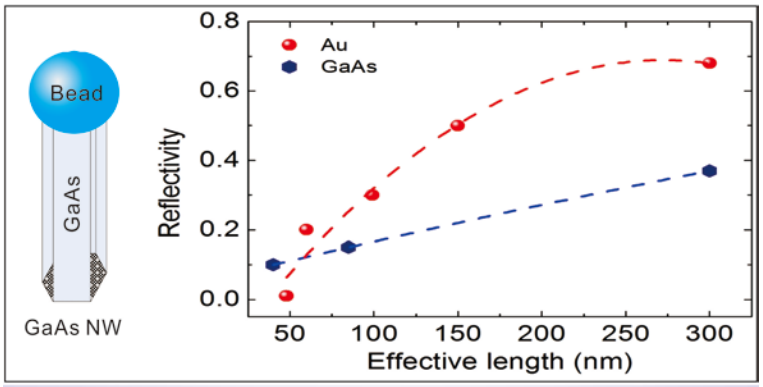

Fluence (mJ/cm^2)	5.5	7	19.5	23.5	29	34.5	37.5	40
Diameter (nm)	96	102	108	123	138	165	180	190
Effective length (nm)	69	82	86	98	110	132	144	152
Au %	100	63	50	34	24	14	11	9
Reflectivity Au	0.18	0.23	0.26	0.31	0.36	0.45	0.49	0.51
Reflectivity GaAs	0.13	0.14	0.15	0.16	0.18	0.20	0.21	0.22

Fig. S8. Top: The size-dependent reflectivity of Au and GaAs (9-15). Bottom: The reflectivity of Au and GaAs adjusted according to their actual size observed in the experiment. To simplify the theoretical modeling, a cube-shaped top bead for the corresponding spherical volume was assumed. The diameter of the bead was converted to the effective length of the cube. The gold percentage was estimated by the ratio of the initial gold volume to the final bead volume.

According to the TTM with a laser beam along the z-axis, the evolution of the electron temperature $T_e(z,t)$ and the lattice temperature $T_L(z,t)$ follows (16-18),

$$C_e \frac{\partial}{\partial t} T_e(z,t) = \frac{\partial}{\partial z}\left(k_e \frac{\partial}{\partial z} T_e(z,t) \right) - g[T_L(z,t) - T_e(z,t)] + S(z,t)$$

$$C_L \frac{\partial}{\partial t} T_L(z,t) = -g[T_e(z,t) - T_L(z,t)] \tag{5}$$

where C_L is the specific heat for phonons, and $S(z,t)$ is the incident laser pulse profile. At a low laser excitation fluence, one usually assumes that the electron/phonon coupling g is a constant, the specific heat C_e for electrons has linear dependence on electron temperature, and the electronic thermal conductivity k_e is approximated by $K_e T_e / T_L$. Such approximations have shown to be inaccurate for electron temperature beyond 3000 K. Here we use the following improved formulae for their temperature dependence,

$$k_e = \frac{4.26\times10^{13} T_e}{1.20\times10^{7} T_e^2 + 1.23\times10^{11} T_L} \tag{6}$$

and Padé approximation for the electron/phonon g and C_e, respectively,

$$g = 1.0 \times 10^{17} \frac{\sum_{n=0}^{4} A_1(n)(T_e/10^4)^n}{1+\sum_{n=1}^{4} A_2(n)(T_e/10^4)^n}$$

$$C_e = 1.0 \times 10^{17} \frac{\sum_{n=0}^{3} B_1(n)(T_e/10^4)^n}{1+\sum_{n=1}^{3} B_2(n)(T_e/10^4)^n} \tag{7}$$

where $A_1(0) = 0.257$, $A_1(1) = -0.549$, $A_1(2) = 0.553$, $A_1(3) = -0.650$, and $A_1(3) = 6.269$; $A_2(1) = -2.544$, $A_2(2) = 4.566$, $A_2(3) = -1.479$, and $A_2(4) = 2.541$; $B_1(0) = -0.043$, $B_1(1) = 8.451$, $B_1(2) = -28.797$, and

$B_1(3) = 68.387$; $B_2(1) = -1.645$, $B_2(2) = 2.539$, and $B_2(3) = 0.702$. All other relevant parameters for Au and GaAs are listed in Fig. S8.

For laser heating of a GaAs NW with an incident intensity profile $I(z,t)$, we employed three-temperature model (3TM) that describes time evolution of four subsystems, namely, the charge carrier density $N_C(z,t)$, and three subsystem temperatures such as carrier temperature, optical and acoustic phonon temperatures. Defining the internal energy for the charge carriers $U_C(z,t)$, and the internal energy for the longitudinal optical (LO) phonons $U_O(z,t)$ and the longitudinal acoustic (LA) phonons $U_A(z,t)$, one has (19-21),

$$\frac{\partial}{\partial t}N_C(z,t) = \frac{\alpha_1 I(z,t)}{\hbar\omega} - \gamma_A N_C^3(z,t)$$

$$\frac{\partial}{\partial t}U_C(z,t) = \frac{\partial}{\partial z}\left[k_C \frac{\partial}{\partial z}T_C(z,t)\right] + \alpha_1 I(z,t) - \frac{3k_B N_C(z,t)}{2}\left[\frac{T_C(z,t) - T_O(z,t)}{\tau_{C-O}}\right] - \frac{3k_B N_C(z,t)}{2}\left[\frac{T_C(z,t) - T_A(z,t)}{\tau_{C-A}}\right]$$

$$\frac{\partial}{\partial t}U_O(z,t) = \frac{3k_B N_C(z,t)}{2}\left[\frac{T_C(z,t) - T_O(z,t)}{\tau_{C-O}}\right] - C_O\left[\frac{T_O(z,t) - T_A(z,t)}{\tau_{O-A}}\right]$$

$$\frac{\partial}{\partial t}U_A(z,t) = \frac{\partial}{\partial z}\left[k_A \frac{\partial}{\partial z}T_A(z,t)\right] + \frac{3k_B N_C(z,t)}{2}\left[\frac{T_C(z,t) - T_A(z,t)}{\tau_{C-A}}\right] + C_O\left[\frac{T_O(z,t) - T_A(z,t)}{\tau_{O-A}}\right] \quad (8)$$

where the internal energies for the carriers, the LO phonons and the acoustic phonons are given by,

$$U_C = N_C E_g + C_C T_C$$

$$U_O = C_O T_O$$

$$U_A = C_A T_A \quad (9)$$

The relevant physical parameters for the 3TM, their nomenclature and their dependence on temperature and carrier density are given in Table S2.

Table S2. The parameters of GaAs used in the three-temperature model.

Physical Property	Value	Reference
Heat capacity of carriers C_C (J/m^3 K)	$C_C = 3N_C k_B$	(21)
Heat capacity of LO phonons C_{LO} (J/m^3 K)	$C_{LO} = 3.06 \times 10^5 - 2.4 \times 10^4 (\theta_{LO}/T_O)^{1.94}$ where θ_{LO}= 344 K	(20, 22)
Heat capacity of acoustic phonons C_A (J/m^3 K)	$C_A = 9.17 \times 10^5 - 4.40 \times 10^4 (\theta_D/T_A)^{1.948}$ where Debye temperature θ_D= 344 K	(21, 22)
Thermal conductivity of carriers k_C (W/m K)	$k_C = 2.5 \times N_C {k_B}^2 \tau_m T_C/m^*$ where m^*= 0.066 m_e, τ_m= 0.3 ps	(20, 23)
Thermal conductivity of acoustic phonons k_A (W/m K)	$k_A = 4.0 \times 10^4/{T_A}^{1.2}$	(20, 24)
Energy relaxation time between carriers and LO phonons τ_{C-O}	$\tau_{C-O} = 0.1 \times 10^{-12}$ (s)	(25)
Energy relaxation time between carriers and acoustic phonons τ_{C-A}	$\tau_{C-A} = 0.5 \times 10^{-12}[1 + (N_C/N_O)^2]$ where $N_O = 2 \times 10^{27}$ (1/m^3)	(20, 21)

Energy relaxation time between LO and acoustic phonons τ_{O-A}	$\tau_{O-A} = 8 \times 10^{-12}$ (s)	(20, 26)
Absorption coefficient α_1 (1/m)	$\alpha_1 = 3.48 \times 10^6 \exp[1.71 \times (x - 1.83)]$ $x = \hbar\omega + E_g(300) - E_g(T_p)$ (eV)	(24)
Auger coefficient γ_A (m^6/s)	$\gamma_A = 1.0 \times 10^{-43}$	(27, 28)
Band gap E_g (eV)	$E_g(T_p) = 1.575 - 0.15(T_p/300)$	(24, 29)
Linear thermal expansion coefficient β	$\beta = 5.7 \times 10^{-6}$ (K^{-1})	(30)
Ga-As interatomic distance ℓ	ℓ = 4.00 Å	(31)
Sound velocity v_s	v_s = 4730 m/s	(32)

Quantitative analysis for the eutectic growth of alloy phases

1. Laser fluence at 5.5 mJ/cm^2

From our studies we could extract some important thermal properties which have not been tabulated in the literature, such as latent heat and heat capacity for the alloy phases during the eutectic growth upon laser heating of the Au/GaAs NWs. To facilitate quantitative analysis of the experimental data including the length reduction of the GaAs NW and the size increment of the bead after each laser pulse, we have employed TTM for gold and 3TM for GaAs to estimate the heat energy absorbed by the NW and the bead upon each laser pulse excitation at a given fluence. According to our simulation, after the 1st laser pulse with a fluence of 5.5 mJ/cm^2, the calculated lattice temperatures for the Au bead (566

K) and the GaAs NW (574 K) are above the temperature of ~555 K needed for the Au_7Ga_2 phase formation. Therefore, at this fluence those Ga atoms from the disappearing NW volume, corresponding to a length reduction of 25 nm and a hexagonal cross section with a side length of 54 nm, are expected to undergo the reaction with the encapped Au atoms at the tip to form Au_7Ga_2 alloy. The excessive heat energy above the temperature (555 K) from the tip and the NW allows us to estimate the latent heat for the alloy formation. Based on the parameters including the molar volumes (Au: 1.0×10^{-5} m^3/mol, GaAs:2.7×10^{-5} m^3/mol), the heat capacities (Au: 2.49×10^6 J/m^3.K, GaAs: 1.76×10^6 J/m^3.K) (31, 33), the densities (Au: 1.93×10^4 kg/m^3, GaAs: 5.32×10^3 kg/m^3, Au_7Ga_2: 1.67×10^4 kg/m^3) (34) and the molar ratio of 7:2 for Au_7Ga_2, we obtained the latent heat of 8 kJ/mol for the Au_7Ga_2 alloy.

After the 2nd laser pulse at the same fluence but with a larger bead of a mixture of gold and alloy, we observed an additional 3 nm length reduction for the NW. According to the 3TM modeling, we obtained a lattice temperature of 574 K for the GaAs NW. For the top bead, the calculated lattice temperatures were 510 and 567 K when 100% gold and 100% GaAs were assumed in the bead, respectively. Using these temperature values and the molar percentage in the bead, we obtained the absorbed heat from the additional bead volume and from the NW with the values of 1.5×10^{-14} J and 1.1×10^{-14} J, respectively. We defined the net heat as the energy needed to raise the bead for the volume reduction in the NW (3 nm times the hexagonal cross-section area of the NW) from room temperature to 555 K. This net heat was calculated from the overall absorbed heat of the bead and the NW subtracting two parts: first, the heat for raising the temperature to 555 K for the gold molar volume (a 7/2 ratio times the Ga molar volume from the reduction of the NW volume); second, the latent heat of the corresponding Ga molar volume from the reduction of the NW volume. Knowing the density of Au_7Ga_2, the specific heat of the Au_7Ga_2 alloy was estimated to be 62 J/mol.K.

After the 3rd laser pulse at the same fluence, we observed 1 nm length reduction for the NW. Following the similar approach, a lattice temperature of 574 K for the GaAs NW was obtained. The calculated lattice temperatures of the top bead were 507 and 567 K when 100% gold and 100% GaAs were assumed, respectively. Using the similar procedures outlined above, we extracted the specific heat for the Au_7Ga_2 alloy to be 60 J/mol.K, which is close to the value obtained from the 2nd pulse laser heating.

2. Laser fluence at 7 mJ/cm^2

After three laser pulses at 5.5 mJ/cm^2, the NW length was shortened by 25, 3 and 1 nm sequentially, and the bead stopped to grow. To continue the reaction dynamics, the laser fluence was increased to 7 mJ/cm^2. Using the similar simulation approach and the experimental observation of a further 10 nm length reduction of the NW, we obtained the lattice temperatures of 658 K for the GaAs NW, 587 K for a 100% gold bead and 649 K for a 100% GaAs bead, and the overall effective temperature was above the temperature of ~620 K needed for AuGa phase. The absorbed energies from the volume reduction of the NW and from the bead with a mixed composition are 4.8×10^{-14} J and 5.3×10^{-14} J, respectively. To calculate the latent heat of AuGa, one needs to deduct the latent heat of Au_7Ga_2 phase and also the energy needed to raise the alloy from room temperature to 620 K for AuGa. These two parts of heat to be subtracted from the overall absorbed laser heat is 2.3×10^{-14} J. Using the density of 1.28×10^4 kg/m^3 for AuGa (34), its latent heat was estimated to be about 21 kJ/mol.

After the 2nd laser pulse at the same fluence, a 3 nm length reduction of the NW was further observed. Based on the 3TM modeling, the lattice temperature of the GaAs NW is found to be 658 K. For the top bead, the calculated lattice temperatures are 571 K for a 100% Au bead and 645 K for a 100% GaAs bead, respectively. Using these temperature values and the molar percentage in the bead, we

estimated the absorbed heat from the additional bead volume and from the NW to be 6.6×10^{-15} J and 4.8×10^{-15} J, respectively. According to the similar procedures mentioned above, we obtained the net heat of 4.65×10^{-15} J. Knowing the density of AuGa, its specific heat of about 41 J/mol.K was obtained.

Supporting References

1. Chen B, Gao Q, Chang L, Wang YB, Chen ZB, Liao XZ, Tan HH, Zou J, Ringer SP, Jagadish C (2013) Attraction of semiconductor nanowires: An in situ observation. *Acta Mater*. 61:7166-7172.
2. Cooke CJ, Hume-Rothery W (1966) The equilibrium diagram of the system gold-gallium *J Less-Common Met* 10:42-51.
3. Elliott RP, Shunk FA (1981) The Au-Ga (gold-gallium) system. *Bull Alloy Phase Diagr* 2:356-357.
4. Leung S, Milnes AG (1982) X-ray diffraction (pole figure) study of the epitaxy of gold thin films on GaAs. *MRS Online Proceedings Library* 18:109.
5. Harmand JC, Patriarche G, Péré-Laperne N, Mérat-Combes M-N, Travers L, Glas F (2005) Analysis of vapor-liquid-solid mechanism in Au-assisted GaAs nanowire growth. *Appl. Phys. Lett.* 87:203101.
6. Stanchina WE, Whelan JM (1983) Solubility of GaAs in Au-Ge eutectic melts. *Solid-state Electron* 26:817-819.
7. Mueller CH, Holloway PH, Connell RG (1992) The ternary phase diagram for Au-Ga-As using the flow chart technique. *MRS Proc* 260:481.

8. Wang J, Liu YJ, Liu LB, Zhou HY, Jin ZP (2011) Thermodynamic assessment of the Au-Ga binary system. *CALPHAD.* 35:242-248.
9. Loebich O (1972) The optical properties of gold: A review of their technical utilization. *Gold Bull* 5:2-10.
10. Huang X, El-Sayed MA (2010) Gold nanoparticles: Optical properties and implementations in cancer diagnosis and photothermal therapy. *J Adv Res* 1:13-28.
11. Kats MA, Blanchard R, Genevet P, Capasso F (2013) Nanometer optical coatings based on strong interference effects in highly absorbing media. *Nat Mater* 12:20-24.
12. Philipp HR, Ehrenreich H (1963) Optical properties of semiconductors. *Phys Rev* 129:1550-1560.
13. Gu Z, Prete P, Lovergine N, Nabet B (2011) On optical properties of GaAs and GaAs/AlGaAs core-shell periodic nanowire arrays. *J Appl Phys* 109:064314.
14. Guo H, Wen L, Li X, Zhao Z, Wang Y (2011) Analysis of optical absorption in GaAs nanowire arrays. *Nanoscale Res Lett* 6:617.
15. Hu S, Chi CY, Fountaine KT, Yao M, Atwater HA, Dapkus PD, Lewis NS, Zhou C (2013) Optical, electrical, and solar energy-conversion properties of gallium arsenide nanowire-array photoanodes. *Energy Environ Sci* 6:1879-1890.
16. Anisimov SI, Kapeliovich BL, Perel'man TL (1974) Electron emission from metal surfaces exposed to ultrafast laser pulses. *Sov Phys JETP* 39:375-377.
17. Tang J (2008) Coherent phonon excitation and linear thermal expansion in structural dynamics and ultrafast electron diffraction of laser-heated metals. *J Chem Phys* 128:164702.
18. Chen J, Chen WK, Tang J, Rentzepis PM (2011) Time-resolved structural dynamics of thin metal films heated with femtosecond optical pulses. *Proc Natl Acad Sci USA* 108:18887-18892.

19. Tien CL, Majumdar A, Gerner FM. Micro-scale Energy Transport (Taylor & Francis, Washington D.C., 1998).
20. Fushinobu K, Majumdar A, Fujikata K (1995) Heat generation and transport in submicron semiconductor devices. *J Heat Transfer* 117:25-31.
21. Lee SH, Lee J, Kang KG, Lee JS (2006) Three-temperature modeling of carrier-phonon interactions in thin GaAs film structures irradiated by picosecond pulse lasers. *J Mech Sci Technol* 20:1292-1301.
22. Kittel C. Introduction to Solid State Physics (6^{th} ed., Wiley, New York, 1986).
23. Bhandari CN, Rowe DM. Thermal Conduction in Semiconductors (Wiley, New York, 1988).
24. Meyer JR, Kruer MR, Bartoli FJ (1980) Optical heating in semiconductors: Laser damage in Ge, Si, InSb and GaAs. *J Appl Phys* 51:5513-5522.
25. Collins CL, Yu PY (1984) Generation of nonequilibrium optical phonons in GaAs and their application in studying intervalley electron-phonon scattering. *Phys Rev B* 30:4501-4515.
26. Lugli P, Bordone P, Reggiani L, Rieger M, Kocevar P, Goodnick SM (1989) Monte Carlo studies of nonequlibrium phonon effects in polar semiconductors and quantum wells: I. Laser photoexcitation. *Phys Rev B* 39:7852-7865.
27. Benz G, Conradt R (1977) Auger recombination in GaAs and GaSb. *Phys Rev B* 16:843.
28. Steiauf D, Kioupakis E, Van de Walle CG (2014) Auger recombination in GaAs from first principles. *ACS Photonics* 1:643-646.
29. Neuberger M. Handbook of Electronic Materials (IFI/Plenum, New York, 1970), Vol. 2.
30. Blakemore JS (1982) Semiconducting and other major properties of gallium arsenide. *J Appl Phys* 53:R123-181.

31. Yao H, Yau SL, Itaya K (1996) In situ scanning tunneling microscopy of GaAs (001), (111)A, and (111)B surfaces in sulfuric acid solution. *Appl Phys Lett* 68:1473-1475.
32. Adachi S. GaAs and Related Materials: Bulk Semiconducting and Superlattice Properties (World Scientific Publishing, Singapore, 1994).
33. Hohlfeld J, Wellershoff SS, Güdde J, Conrad U, Jähnke V, Matthias E (2000) Electron and lattice dynamics following optical excitation of metals. *Chem Phys* 251:237-258.
34. Froemel J. Gallium-based solid liquid interdiffusion bonding of semiconductor substrates near room temperature (Dissertation, Technische Universität Chemnitz, 2015).